Stability analysis of separated flows subject to control by zero-net-mass-flux jet

Olaf Marxen, Rupesh B. Kotapati, Rajat Mittal, and Tamer Zaki

Citation: Physics of Fluids (1994-present) **27**, 024107 (2015); doi: 10.1063/1.4907362
View online: http://dx.doi.org/10.1063/1.4907362
View Table of Contents: http://scitation.aip.org/content/aip/journal/pof2/27/2?ver=pdfcov
Published by the AIP Publishing

PHYSICS OF FLUIDS **27**, 024107 (2015)

Stability analysis of separated flows subject to control by zero-net-mass-flux jet

Olaf Marxen,[1,a)] Rupesh B. Kotapati,[2,b)] Rajat Mittal,[2] and Tamer Zaki[1,2,c)]
[1]*Department of Mechanical Engineering, Imperial College London, Exhibition Road, South Kensington, London SW7 2AZ, United Kingdom*
[2]*Department of Mechanical Engineering, Johns Hopkins University, 3400 North Charles Street, Baltimore, Maryland 21218, USA*

(Received 3 June 2014; accepted 5 January 2015; published online 17 February 2015)

The control of flow around a canonical airfoil-like geometry with laminar separation bubble is analyzed using linear stability theory. The theoretical predictions are compared to data from Navier-Stokes simulations [Kotapati *et al.*, "Nonlinear dynamics and synthetic-jet-based control of a canonical separated flow," J. Fluid Mech. **654**, 65-97 (2010)], in which the flow was controlled through a zero-net-mass-flux actuator. Very good agreement between the two approaches is found for a range of frequencies from low to high relative to the most dominant frequency for convective instability. The uncontrolled case exhibits periodic vortex shedding from the separation bubble due to an absolute instability. Linear modes with intermediate frequencies are found to exhibit strongest convective amplification, and forcing at these frequencies is most effective in order to reduce the size and extent of the separation bubble. The corresponding physical mechanism relies on a Kelvin-Helmholtz instability of the separated shear layer in conjunction with the non-linear effect of the mean flow deformation. For low frequencies, the front part of the bubble still diminishes due to the interaction of a vortex that starts from the actuator with the wall. This vortex transiently amplifies downstream due to the Orr mechanism. Actuation at high frequencies leads to visible, amplified instability waves in the shear layer, but is not effective in reducing the size of the bubble.
[http://dx.doi.org/10.1063/1.4907362]

I. INTRODUCTION

Laminar separation bubbles (LSBs) may occur due to strong adverse pressure gradients,[1–5] for instance on the surface of slender bodies such as laminar airfoils or in turbomachinery applications.[6–8] As a result, they often strongly affect the airfoil performance, such as lift and drag, as well as noise production. For essential features of LSBs, see Marxen and Henningson.[9]

Control of laminar separation using zero-net-mass-flux (ZNMF) devices for airfoils operating at low to medium Reynolds numbers is a common approach in both numerical[10,11] and experimental[12,13] investigations. However, ongoing physical processes in such flows can be diverse, spanning from convective-type (Kelvin-Helmholtz) instability[14,15] to vortex-wall interaction.[16] This diversity complicates the choice of important parameters for effective control, such as actuator amplitude, frequency, and location. A better understanding of these physical processes is sought in this work and is expected to help improve the efficiency of future active flow-control devices.

While the physical processes occurring when varying the *forcing amplitude* are well understood,[9,17] the effect of frequency variation is less clear. Using hot-wire anemometry and surface pressure measurements to study laminar boundary-layer separation on an airfoil, Yarusevych *et al.*[18] found that "the optimum excitation frequency for acoustic boundary layer control matches that of

[a)]Current address: Mechanical Engineering Sciences, University of Surrey, Guildford GU2 7XH, United Kingdom.
[b)]Current address: Aerodynamics Validation, Exa Corporation, MA 01803, USA.
[c)]Author to whom correspondence should be addressed. Electronic mail: t.zaki@jhu.edu

the most amplified disturbance in the separated shear layer" and they suggested that "linear stability theory may be used to predict optimum excitation parameters." Simoni *et al.*[19] performed a linear stability analysis for a laminar separated flow and found a wide range of unstable frequencies, including low-frequency perturbations. However, their analysis was based on a piecewise linear profile instead of an actual measured or simulated velocity profile. Rist and Augustin[11] reported a change in bubble size with forcing frequency, but they only investigated two different frequencies that were close to the most amplified frequency for a very small forcing amplitude.

In order to better characterize the relevant physical processes, we analyze a set of flow fields that were computed by Navier-Stokes (NS) simulations.[1] We perform a comparison of Fourier analysis of the NS fields and results from local linear stability theory based on the Orr-Sommerfeld equation. Previous investigations have shown that local linear stability theory (LST) very accurately reproduces convective growth rates and amplitude functions for flows with laminar separation if the disturbance frequency is within the range of integrally most amplified frequencies,[15] although some evidence exists that LST may work well for higher and lower frequencies.[20] Here, it will be verified that LST is a suitable method of analysis for a much wider range of frequencies, including significantly higher and lower frequencies than previously considered.

This paper is organized as follows: first, the flow configuration and the mean flows obtained for different ZNMF frequencies are described in Sec. II. These mean flows serve as a base state for subsequent stability analyses. Next, the linear stability analysis is described (Sec. III). The post-processing procedures applied to time-dependent numerical data are also reported in the same section. In Sec. IV, stability characteristics of the different mean flows are presented, and in Sec. V Fourier analysis of numerical data is compared with the theoretical results. Based on this comparison, a discussion of the active physical mechanisms is presented, and is followed by conclusions in Sec. VII.

II. FLOW CONFIGURATION AND MEAN FLOW FIELDS

The general setup is a finite-length flat plate with an elliptic leading edge placed in a channel with slip walls, subject to a uniform incoming free stream at the channel inlet (Figure 1). The leading edge of the plate is located at $x = 0$. Steady blowing and suction with a peak suction velocity of $0.8U_\infty$ are applied on the upper (slip) wall of the channel within the interval $0.7 < x/c < 1.3$, which induces an adverse pressure gradient (APG) along the top wall of the flat plate. The APG leads to separation of the laminar boundary layer on the upper surface of the plate, followed by unsteady vortex shedding. The latter causes the separated shear layer to reattach in the mean sense.

All quantities are non-dimensionalized with the inlet velocity U_∞ and the chord of the plate c. The corresponding Reynolds number is $Re_\infty = U_\infty c/\nu = 60{,}000$. The origin of the vertical coordinate, $y = 0$, lies on the upper surface of the flat plate, and the streamwise origin corresponds to the start of the plate, i.e., the elliptic nose. The flat part of the plate starts at $x/c = 0.2$. In the following, we focus solely on the region around the separation bubble, which is located in the flat section downstream of the elliptic leading edge and upstream of the end of the plate, namely, $0.2 < x/c < 1.0$.

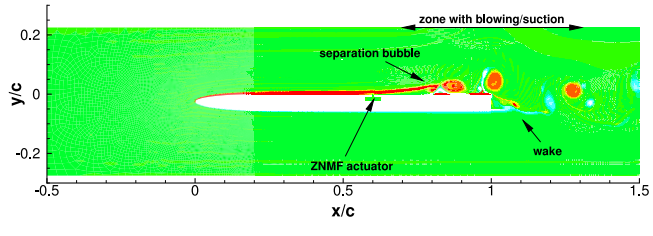

FIG. 1. Computational setup for the Navier-Stokes simulations of LSB and flow response to ZNMF forcing. In the figure, ZNMF actuator, blowing/suction zone, separation bubble, and wake of the airfoil are specified.

TABLE I. Overview of simulation cases: actuation frequencies F_J^+ and respective time-averaged results (x_S: separation point; x_R: reattachment point; H_{sep}: bubble height). In our nomenclature, SJ stands for forcing by ZNMF jet and the subscript denotes the forcing frequency.

Case	$F_J^+ = f_J c/U_\infty$	x_S	H_{sep}	x_R	$x_R - x_S$
$0/noSJ$		0.638	0.0337	0.973	0.335
$1/SJ_{F0.725}$	0.725	0.668	0.0288	0.970	0.302
$2/SJ_{F0.967}$	0.967	0.666	0.0255	0.966	0.3
$3/SJ_{F1.45}$	1.450	0.672	0.0190	0.943	0.271
$4/SJ_{F2.9}$	2.900	0.678	0.0152	0.922	0.2444
$5/SJ_{F3.625}$	3.625	0.683	0.0125	0.899	0.216
$6/SJ_{F5.8}$	5.800	0.668	0.0152	0.854	0.186
$7/SJ_{F8.7}$	8.700	0.647	0.0344	0.980	0.334
$8/SJ_{F11.6}$	11.600	0.644	0.0341	0.978	0.334

A ZNMF actuator is centered at $x/c = 0.6$. This actuator is used to diminish boundary-layer separation downstream of its location by forcing at a fixed frequency and amplitude. Several different non-dimensional frequencies $F_J^+ = f_J c/U_\infty$ were examined, while the amplitude was kept constant. Table I specifies forcing frequencies and designations of the different cases. Case 0 refers to an undisturbed flow where the ZNMF actuator is inactive (Figure 3(a)). The pressure profile on the top boundary depends on the control. Resulting wall-pressure distributions (c_p) are provided in Figure 12 by Kotapati *et al.*[1] and are therefore not repeated here.

The designation for different cases follows the one adopted by Kotapati *et al.*[1] who considered the same configuration investigated here. We use their numerical data in order to perform a stability analysis and to compare theoretical and numerical results. The flow field was simulated using a second-order finite-volume algorithm, and the numerical details are provided in the work by Kotapati *et al.*[21] The spatial resolution adopted in the numerical simulation is specified in Table 1 by Kotapati *et al.*[1] Their simulations with two different grids showed excellent agreement with one another, with a variability of less than 1% for mean-flow quantities.[1] In this way, Kotapati *et al.*[1] could establish "the grid independency of the simulation results with respect to the characteristic frequency scales." For this setup, two- and three-dimensional Navier-Stokes simulations were performed. Throughout this paper, only results from two-dimensional Navier-Stokes simulations are considered for two reasons: first, similar spectral dynamics and lock-on states were observed for both the two-dimensional and three-dimensional simulations[22] and second, two-dimensional waves are most important here since the actuators used for flow control were two-dimensional in both the two- and three-dimensional simulations. In Kotapati *et al.*[22], it was demonstrated that the three-dimensional large-eddy simulation (LES) and two-dimensional direct simulations are qualitatively similar. In addition, in the presence of forcing, the 3D LES became more akin to the

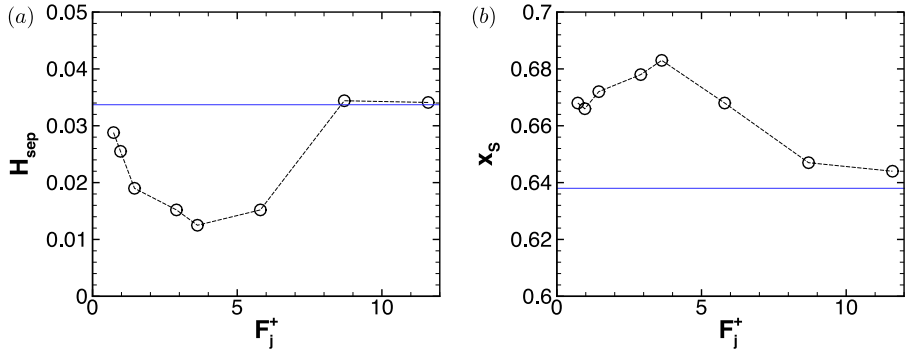

FIG. 2. Mean flow quantities as a function of forcing frequencies: (a) maximum height of the separation bubble H_{sep} and (b) streamwise point of separation x_S. For reference, results from the uncontrolled case are marked by horizontal lines.

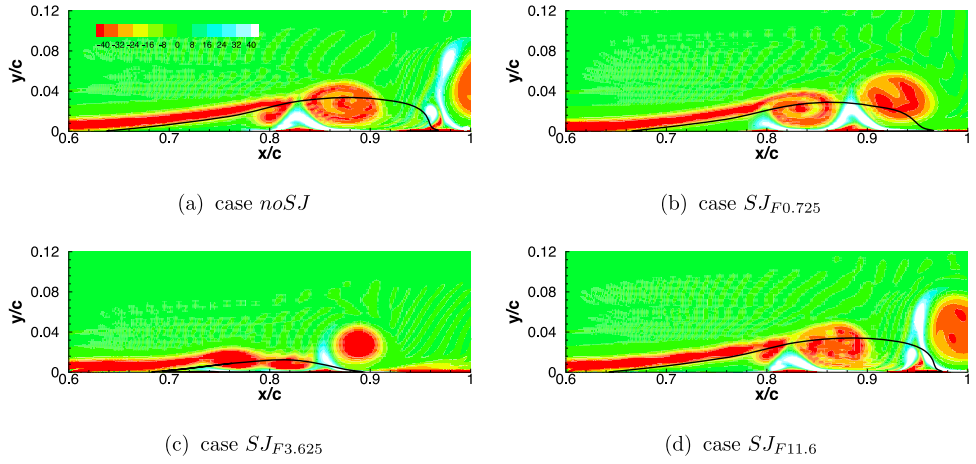

(a) case $noSJ$ (b) case $SJ_{F0.725}$

(c) case $SJ_{F3.625}$ (d) case $SJ_{F11.6}$

FIG. 3. Vorticity contours for Navier-Stokes simulation, together with mean dividing streamline. This streamline originates at the wall at the streamwise point of separation x_S (depicted for all cases in Figure 2(b)) and possesses a maximum distance from the wall H_{Sep} (see Figure 2(a)).

two-dimensional flow. The analysis of the 2D base state from the direct simulations is therefore appropriate for the purposes of the current study. In the herein performed linear stability analyses, we limit ourselves to the exponential growth of two-dimensional disturbances. Due to this restriction, three-dimensional dynamics that can become relevant in the aft portion of the bubble are excluded.

Data from cases 0 through 8 are examined herein with respect to their stability properties and disturbance evolution. The goal of the analysis is to develop a deeper understanding of the physical processes which take place in the controlled flow fields.

For most frequencies, ZNMF forcing leads to a lower height of the separation bubble (Figure 2(a)). Moreover, the separation point moves downstream (Figure 2(b)). The overall length of the bubble diminishes since the reattachment location moves upstream (see Table I). The main parameters defining the separation bubble in Table I have been taken from Table 1 by Kotapati *et al.*[1] For frequencies in the medium range of the interval considered here ($F_j^+ \approx [2.9, 5.8]$), this effect is particularly strong: the bubble height is lowest and the separation location has moved farthest downstream (Figure 3(c)). This is due to the feedback effect of the mean flow deformation.[9,17] The actuation causes earlier emergence of large-amplitude vortical structures inside the separation bubble leading to early mean reattachment of the separated flow. In turn, the laminar flow upstream is altered via the action of the pressure (via the elliptic influence of the pressure).

For lower frequencies (Figure 3(b)), the bubble height approaches the uncontrolled value (Figure 2(a)). However, the separation location remains farther downstream (Figure 2(b)). This behavior is not consistent with the effect of the mean flow deformation, and a different physical explanation is provided below in Sec. V D. For high forcing frequencies (Figure 3(d)), the bubble remains largely unchanged compared to the uncontrolled case.

III. METHODOLOGY

A. Linear stability theory

The growth of small perturbations in the laminar boundary layer and the separating shear layer is characterized using LST, or precisely the Orr-Sommerfeld equation.[23]

The flow field is decomposed into a known steady base state $U = U(y)$, $V = 0$, and $P = P(y)$ (parallel-flow assumption) and small two-dimensional disturbances $s' = u'$, v', and p'. The Navier–Stokes equations for two-dimensional incompressible flow are then linearized around the

base flow with respect to these disturbances. Assuming a normal-mode *ansatz* for the disturbances,

$$s' = \hat{s}(y)\mathrm{e}^{i(\alpha x-\omega t)}, \quad \hat{s}(y) \in C, \tag{1}$$

the following fourth order ordinary differential equation, known as the Orr–Sommerfeld equation,[23] is obtained:

$$(\alpha U-\omega)\left(\frac{d^2}{dy^2}-\alpha^2\right)\hat{v}-\alpha\frac{d^2U}{dy^2}\hat{v}=-\frac{i}{Re}\left(\frac{d^4}{dy^4}-2\alpha^2\frac{d^2}{dy^2}+\alpha^4\right)\hat{v} \tag{2}$$

with complex α, $\Re(\alpha)$ being the streamwise wave number and $\Im(\alpha)$ the streamwise amplification rate, and complex ω, $\Re(\omega)$ being the circular frequency and $\Im(\omega)$ the temporal amplification rate. Note that for each case, a different base flow is used, namely the time-averaged flow field from the respective simulation. Supplementing Eq. (2) with homogeneous boundary conditions at the wall and at large distances from the wall, and assigning either α or ω, we obtain an eigenvalue problem.

To study convective streamwise amplification of a forced disturbance, the spatial approach, i.e., prescribing $\Re(\omega) = \beta = 2\pi f$ and setting $\Im(\omega) = 0$, is appropriate. In this way, we obtain a complex disturbance spectrum α. Since the only input required for stability analysis is the streamwise base-flow velocity profile $U(y)$ at a certain streamwise location, the analysis is local. With the present definition, for a given disturbance frequency $\Re(\omega)$, the flow is unstable if $\Im(\alpha) < 0$ and stable if $\Im(\alpha) > 0$. Only the non-zero discrete eigenvalue corresponding to the strongest amplification will be considered.

Linear growth rates $\Im(\alpha)$ can be integrated in the downstream direction to provide a measure of the disturbance amplification (amplitude growth),

$$A_s^{LST}(x) = A_{0,s}\exp\{-\int \Im(\alpha(x))dx\}, \tag{3}$$

with arbitrary initial amplitude $A_{0,s}$ based on the respective underlying mean flow and frequency. A different value of this initial amplitude will be chosen for each individual comparison between Navier-Stokes simulations and linear stability theory. This procedure is justified due to the linearity of the theory.

Considering only a single eigenmode from linear stability theory is invalid in the near field of the actuator due to the fact that the actuator excites a whole range of eigenmodes, most of which are rapidly decaying. Only further downstream will the (single) amplified eigenmode govern the flow dynamics. In all cases discussed below, this eigenmode possess a sufficiently small amplitude, at least within a short distance downstream of the actuator, so that a comparison with LST is justified. Moreover, based on previous comparisons between linear stability theory and direct numerical simulations (see for instance, Ref. 24), it is known that results from LST are valid until very close to the saturation region, despite fairly large amplitudes of the instability wave in this region.

B. Post-processing of simulation data: Fourier analysis

For the purpose of comparison to the LST results, the Navier-Stokes simulation data are Fourier analyzed in time with a fundamental circular frequency $\beta_0 = 2\pi(f_a c/U_\infty)$. The non-dimensional frequency $(f_a c/U_\infty)$ is generally chosen to be $F_J^+/2$, i.e., half the forcing frequency F_J^+. In the unforced case it is set to $f_a = 0.3625$, since the observed shedding frequency $F^+ = 2.9$ in the uncontrolled case is a harmonic of this frequency and it also corresponds to half of the forcing frequency for the case with the lowest forcing frequency. The corresponding inverse discrete Fourier transform is

$$s(x,y,t_n) = \frac{1}{N}\sum_{k=0}^{N-1}|\hat{s}_k(x,y)|\cos[k\beta_0 n\Delta t + \Phi_{s,k}(x,y)], \quad n=[0,N-1], \quad s=u,v, \tag{4}$$

where N is the sample size in one forcing period, n is the sampling index, and Δt is the sampling interval so that discrete time $t_n = n\Delta t$. Here, the Fourier coefficients $\hat{s}_k$ are complex, $\hat{s}_k = \hat{s}_{k,r} + i\hat{s}_{k,i}$,

with amplitude A_s and phase Φ_s defined as

$$A_s(x, y, k \text{ or } F^+) = |\hat{s}_k| = \sqrt{\hat{s}_{k,r}^2 + \hat{s}_{k,i}^2}, \tag{5}$$

$$\Phi_s(x, y, k \text{ or } F^+) = \tan^{-1}(\hat{s}_{k,i}/\hat{s}_{k,r}) \text{ with } F^+ = k\beta_0/(2\pi). \tag{6}$$

Instead of k, the value of F^+ is used in the discussion below.

Downstream evolution of the disturbance amplitude in the simulations is quantified and compared to LST. For the Fourier transformed data from the simulations, wall-normal maxima of the amplitudes of the streamwise disturbance velocity are computed as

$$A_s^{max}(x) = \max_y\{A_s(x, y)\} = \max_y\{|\hat{s}_k(x, y)|\}. \tag{7}$$

The time interval for the spectral analysis depended on the case. For the uncontrolled flow, the lowest frequency considered in the Fourier analysis was $F_{low}^+ = 0.3625$, which was resolved with 138 time steps, and the highest frequency was $F^+ = 8.7$, resolved with only 5.75 time steps. In case $SJ_{0.725}$, the lowest frequency is $F_{low}^+ = 0.365$ and spans 68 time steps. In case $SJ_{11.6}$, the lowest frequency is $F_{low}^+ = 1.45$ and is spanned by 344 time steps. For the Fourier analysis at the forcing frequency, typically around 30-40 time steps were used.

IV. RESULTS FROM LINEAR STABILITY THEORY

A. Stability diagrams

An overview of the LST results is shown in the stability maps in Figure 4. The linear exponential growth rates are computed for the time-averaged flow fields of four cases: *noSJ*, $SJ_{F0.725}$, $SJ_{F3.625}$, and $SJ_{F11.6}$. The adverse pressure gradient starts to affect the boundary layer evolution from approximately $x = 0.42$ onwards, and in this region the boundary layer profiles are inflectional. Indeed, downstream of this location we observe a widening of the region of neutral stability. The region includes increasingly more unstable frequencies due to an inviscid Kelvin-Helmholtz-type instability caused by these inflectional profiles (further evidence for this conjecture regarding the stability mechanism is provided in Sec. V C). In order to further investigate the effect of viscosity, we performed a stability analysis at artificially increased Reynolds number for the same base-flow profile. We could confirm that the instability persists in the high *Re* limit, which supports our assertion that we have an inviscid instability. The growth rate was seen to increase with increasing Reynolds number, i.e., as the influence of viscosity was diminished.

It is instructive to compare the stability diagrams of a forced case, e.g., case $SJ_{F3.625}$ with a forcing frequency $F_j^+ = 3.625$ (Figure 4(c)), and the unforced case (Figure 4(a)). The comparison reveals that the influence of forcing on convective linear instability is particularly strong for frequencies that were originally optimal or associated with the peak amplification in the uncontrolled case $F^+ \approx 6.9$. This conjecture is further confirmed in Figure 5. Qualitatively, this figure resembles Figure 2: those forcing frequencies that strongly reduce the maximum height of the bubble also considerably reduce the frequency of the most amplified disturbance. At the same time, when the minimum frequency is reached, it is close to the forcing frequency of the respective case.

According to Figures 2 and 3(c), the most effective actuation frequency is $F_j^+ = 3.625$ since it leads to the smallest separation bubble. The most amplified linear stability mode at this actuation frequency is given in Figure 5 and is recorded at approximately $F^+ = 4.5$. Figure 5 demonstrates that, in general, the forcing is most effective when its frequency is near that of the most unstable LST mode of the forced flow, although the exact relation requires a better resolution of the frequency range.

B. Amplification rates

Upstream of the actuator position flow stability remains unchanged and hence LST results with and without an active actuator are almost indistinguishable (see Figure 6(a)). However, further downstream of the actuator position and especially inside the separation bubble, the amplification

rate in actuator-controlled cases does not reach the same strongly negative values seen in the uncontrolled flow (*noSJ*). Instead, the overall peak value attained at a certain streamwise position decreases significantly, for instance by 68.1% at $x = 0.7$ in case $SJ_{F3.625}$ (see Figure 6(b)). But even for a fixed frequency, the amplification rate in the controlled cases is significantly lower compared to the uncontrolled case as has been observed by Marxen and Henningson[9] and Marxen and Rist.[17]

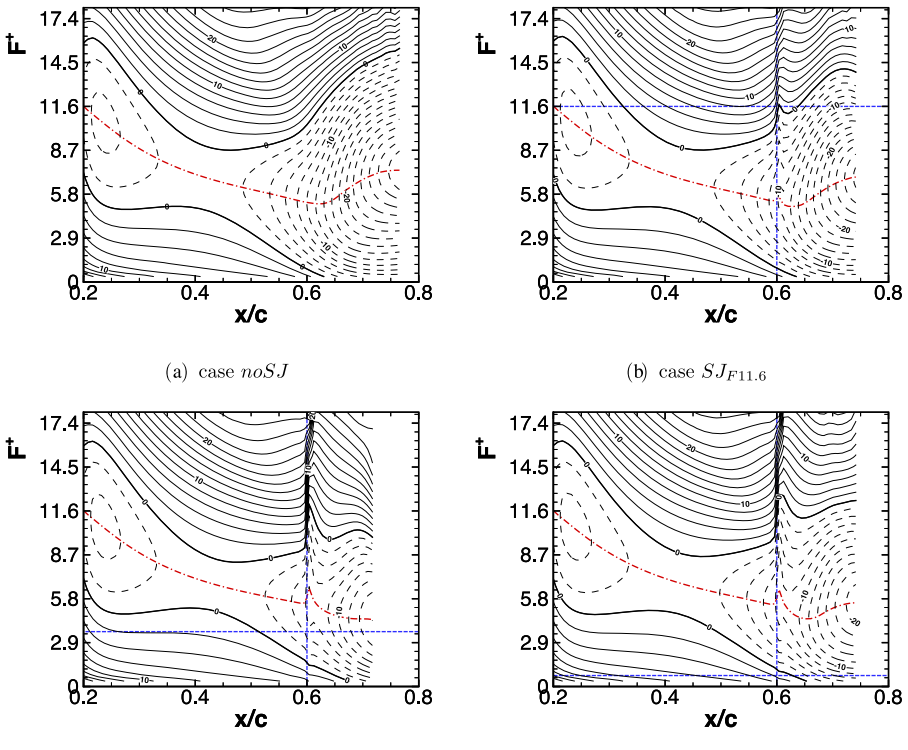

(a) case $noSJ$ (b) case $SJ_{F11.6}$

(c) case $SJ_{F3.625}$ (d) case $SJ_{F0.725}$

FIG. 4. Stability diagrams: Contours of the imaginary part of the smallest eigenvalue α_i computed from Eq. (2). The contour spacing is $\Delta\alpha_i = 2$. The thick, solid line marks the neutral stability curve which corresponds to $\Im(\alpha) = 0$. Thin dashed lines correspond to $\Im(\alpha) < 0$ (amplification). The horizontal and vertical lines in Figures 4(b)–4(d) mark the forcing frequency and actuator location, respectively.

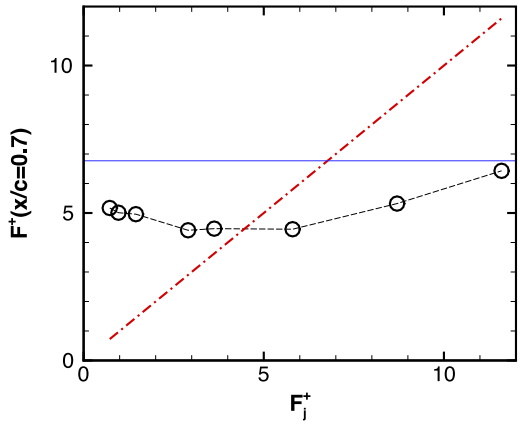

FIG. 5. Most amplified frequency F^+ at the streamwise location $x/c = 0.7$ as a function of forcing frequency F_j^+. The horizontal line marks the most amplified frequency F^+ at the streamwise location $x/c = 0.7$ for the uncontrolled case. The dashed-dotted line corresponds to $F^+ = F_j^+$.

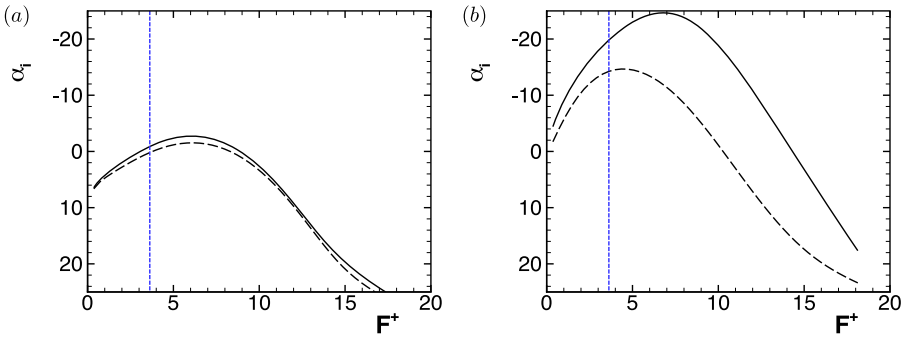

FIG. 6. Amplification rates from linear stability theory for cases *noSJ* (—) and $SJ_{F3.625}$ (– – –) at the streamwise locations (a) $x = 0.5$ and (b) $x = 0.7$. The vertical lines mark the forcing frequency.

For instance, at the forcing frequency of $F_j^+ = 3.625$, the growth rate α_i is reduced by 39.1% compared to case *noSJ*.

Moreover, the frequency of the most amplified disturbance has moved to lower values. The frequency of peak amplification is reduced by 58% from $F^+ = 6.89$ in case *noSJ* to $F^+ = 4.35$ in case $SJ_{F3.625}$. As a result of this shift, the frequency of peak amplification is close to the forcing frequency for case $SJ_{F3.625}$, which possesses the smallest bubble height.

V. THE EFFECT OF FORCING ON DISTURBANCE EVOLUTION

In order to examine the effectiveness of forcing for the control of laminar separation, LST results will be compared to results from Navier-Stokes simulations. The different cases with forcing are classified into three categories according to their forcing frequencies, treated in Secs. V B–V D, respectively. Before we investigate the effect of forcing, we briefly discuss the key characteristics or mechanics of the uncontrolled flow in Sec. V A.

A. Mechanics of the uncontrolled flow

In the uncontrolled case, infinitesimal disturbances are present in the boundary layer and inevitably trigger a convective instability. Depending on its amplitude and frequency, this background noise could either be benign or alter the flow dynamics. Various potential sources may be responsible for this noise. First, disturbances may originate from round-off errors or iteration residuals that are produced by the numerical scheme applied to advance the flow field in time. Second, an absolute instability in the separation bubble could trigger an acoustic feedback loop in conjunction with the production of sound or pressure waves at the airfoil trailing-edge.[25] In connection with receptivity of the elliptical leading edge of the airfoil, this loop could cause convective instability waves in the boundary layer upstream of the separated flow region, in particular at the vortex shedding frequency observed in the separation bubble and in the wake of the airfoil.

Convective instability waves can indeed be detected if the flow field is Fourier analyzed in time, and their downstream evolution in the uncontrolled case is visualized in Figure 7 for the frequency $F^+ = 2.9$. This frequency is much lower than the peak convective frequency seen in Figure 4(a), and it is therefore curious that disturbances with this frequency possess the highest amplitude in the upstream part of the bubble. The most likely source of disturbances with this frequency is the above-mentioned feedback loop. Disturbances with $F^+ = 2.9$ dominate the flow inside and downstream of the bubble (for details see Figure 8 in Ref. 1), and then they trigger corresponding disturbances at the leading edge according to the feedback loop. This loop may explain why they possess a higher amplitude upstream of separation compared to those disturbances at $F^+ = 5.8$ and $F^+ = 8.7$, which are convectively more unstable (see Figure 4(a)). However, since none of the convective waves governs the overall flow dynamics as we will see below, it is not necessary to determine their exact source in the present case.

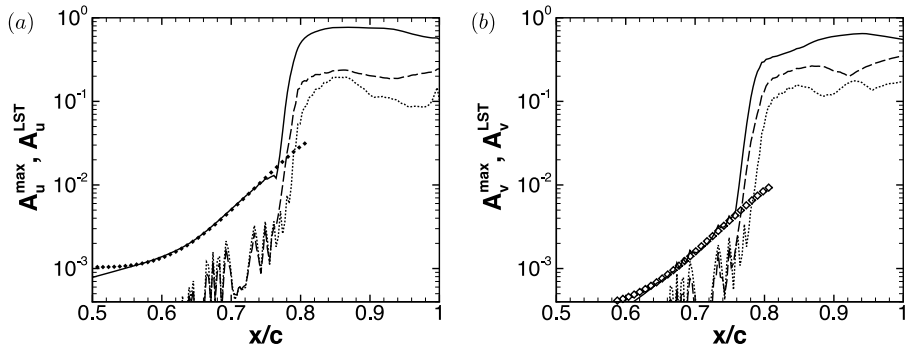

FIG. 7. Case *noSJ*: Amplification curves calculated using Eqs. (3) and (7) for different frequencies, $F^+ = 2.9$ (—); $F^+ = 5.8$ (– – –); $F^+ = 8.7$ (···). Results from LST (Eq. (3)) for $F^+ = 2.9$ are given as symbols and are scaled so that they match the amplitude from the Navier-Stokes simulations in the region of disturbance growth for the (a) streamwise $s = u$ and (b) wall-normal $s = v$ velocity components.

Figure 7 also presents LST results for comparison. The agreement between the theoretically predicted growth and the simulation results is remarkable in the range $0.55 < x < 0.75$ for both the streamwise velocity component (Figure 7(a)) and the wall-normal velocity component (Figure 7(b)), confirming that convective instability waves are present in the upstream part of the separation bubble.

Downstream of $x = 0.75$, an abrupt increase of disturbance amplitude is observed (Figure 7), which is not in agreement with the convective instability predicted by LST. Hence, convective LST can explain initial disturbance growth seen in numerical simulations up to $x = 0.75$, but not the almost explosive growth observed between $x = 0.76$ and $x = 0.8$. This latter growth eventually leads to disturbance saturation and the formation of vortices, which are then periodically shed from the bubble (Figure 1).

The shape of the mean-flow profile in this region indicates that the most likely explanation for such explosive growth is an absolute instability. Based on local linear stability theory, Alam and Sandham[26] found that for a local Reynolds number $Re_{\delta^*} \approx 1600$, which is reached here at $x \approx 0.79$, a mean reverse-flow velocity of $|U_r/U_\infty| = 0.16$ may be sufficient to cause an absolute instability. In fact, such an amount of reverse flow is reached at $x = 0.8$ (Figure 8). Further downstream, even larger reverse-flow velocities are established in the present case. It is therefore concluded that the unforced case exhibits an absolute instability which leads to explosive disturbance growth followed by saturation of the disturbance at $F^+ = 2.9$.

The convective amplification of disturbances seen upstream of the region of absolute instability is likely less influential on the flow dynamics in the uncontrolled case. However, our analysis shows that small-amplitude convectively growing instability waves due to a Kelvin-Helmholtz instability may be present prior to the location of visible unsteadiness. This observation is important since it opens up the possibility to exploit this hydrodynamic instability for flow control.

B. High-frequency forcing: Essentially uncontrolled

When the actuation is at a high frequency (cases with $F_j^+ = 11.6$ and 8.7), a sharp peak in the disturbance amplitude is observed around the location of the actuator (Figure 9(a)). A convectively unstable wave develops within a short distance of the actuator and grows in amplitude further downstream. A comparison with LST for case $SJ_{F11.6}$ shows that the agreement between theoretical and numerical results in the region $0.64 < x < 0.8$ is again very good (Figure 9(a)). However, the disturbance at $F^+ = 2.9$ of case $SJ_{F11.6}$ still exhibits explosive growth and quickly overtakes the forced perturbation (Figure 9(a)). Indeed, when comparing the amplitudes for the frequencies $F^+ = 2.9$ and $F^+ = 5.8$ between cases $SJ_{F11.6}$ and *noSJ* (Figure 9(b)), we can see that the streamwise evolution of maximum amplitude for these frequencies is almost identical in both cases. While the forced disturbance with $F^+ = 11.9$ agrees well with LST, it leaves the flow essentially unaffected. Instead,

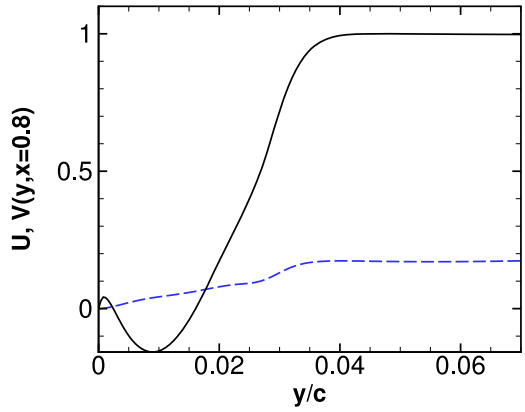

FIG. 8. Streamwise U (—) and wall-normal V (– – –) mean velocity profiles from Navier-Stokes simulation for case *noSJ* at $x = 0.8$, normalized such that the peak of the streamwise velocity component is 1.

the flow dynamics and unsteady processes are governed by the same absolute instability seen in the uncontrolled case as discussed above.

In case $SJ_{F8.7}$ the picture is similar, although not identical (Figure 10). Differences are a less favourable agreement with LST downstream of $x = 0.7$ and a slightly delayed explosive growth of the disturbance with $F^+ = 2.9$. Moreover, the forced disturbance appears to saturate before the disturbance with $F^+ = 2.9$ takes over. Nevertheless, the two cases $SJ_{F11.6}$, $SJ_{F8.7}$ are sufficiently similar so that they can be denoted as essentially uncontrolled due to their strong similarity with the reference case without forcing. This observation can explain why the maximum height of the bubble in both forced cases is almost identical to the uncontrolled case (Figure 2(a)). The slight change of separation location (Figure 2(b)) may be due to direct non-linear effects, since the forcing creates a mean-flow distortion adjacent to the actuator location due to the quadratic non-linearity of the Navier-Stokes equations.

C. Intermediate forcing frequency: Control by a Kelvin-Helmholtz mechanism

The maximum amplitudes for cases $SJ_{F3.625}$ and $SJ_{F2.9}$ are reported in Figure 11. As before, the downstream evolution of the forced perturbation seen in the numerical simulation compares well with LST. Moreover, the flow dynamics are governed by the forced perturbation, which remains large over the entire domain downstream of the actuator.

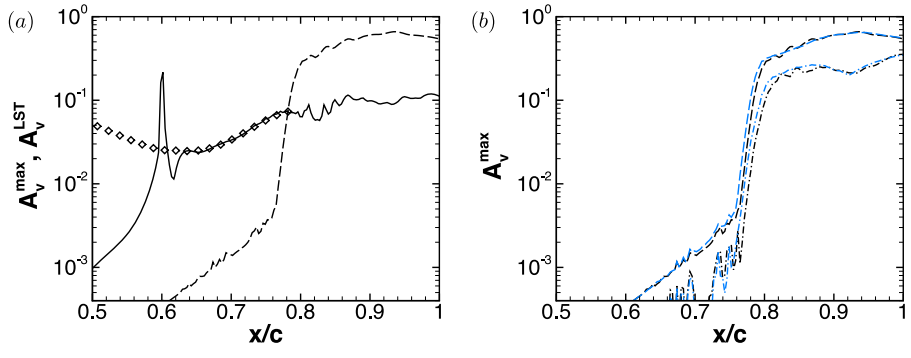

FIG. 9. Case $SJ_{F11.6}$: Amplification curves calculated using Eqs. (3) and (7) for different frequencies. (a) Results from LST (Eq. (3)) for the forcing frequency $F^+ = 11.6$ are given as symbols and are scaled so that they match the amplitude from Navier-Stokes simulation. (a) Navier-Stokes results from case $SJ_{F11.6}$ for $F^+ = 11.6$ (solid line) and $F^+ = 2.9$ (– – –). (b) Comparison between Navier-Stokes results for case $SJ_{F11.6}$ (black lines) and case *noSJ* (grey/blue lines) for $F^+ = 2.9$ (– – –) and $F^+ = 5.8$ (— · —).

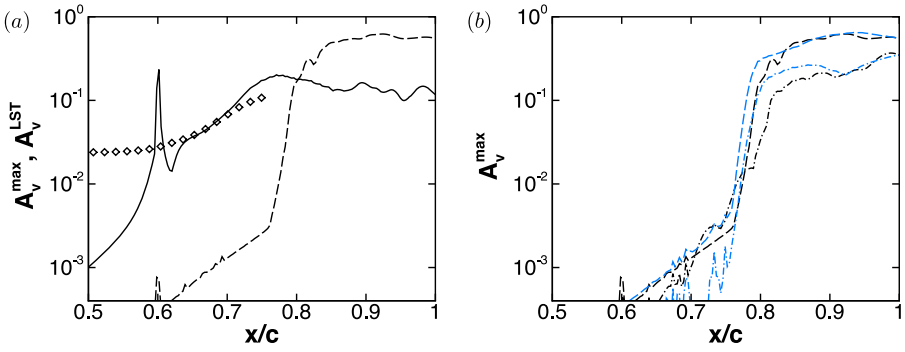

FIG. 10. Case $SJ_{F8.7}$: Amplification curves calculated using Eqs. (3) and (7) for different frequencies. (a) Results from LST (Eq. (3)) for the forcing frequency $F^+ = 8.7$ are given as symbols and are scaled so that they match the amplitude from Navier-Stokes simulation. (a) Navier-Stokes results from case $SJ_{F8.7}$ for $F^+ = 8.7$ (solid line) and $F^+ = 2.9$ (– – –). (b) Comparison between Navier-Stokes results for case $SJ_{F8.7}$ (black lines) and case *noSJ* (grey/blue lines) for $F^+ = 2.9$ (– – –) and $F^+ = 5.8$ (— · —).

Amplitude profiles $A_s(y)$ for the streamwise and the wall-normal velocity components at the forcing frequency are presented in Figure 12(a), while phase profiles $\Phi_s(y)$ are depicted in Figure 13(a). They agree favorably between the Navier-Stokes simulations and LST. It is therefore not surprising that both velocity components eventually attain the same streamwise growth rate (Figure 12(b)). The relation between the maximum of the u and the v amplitude functions is also approximately the same, i.e., $\hat{u}^{max}$ is roughly 2.4 times larger than $\hat{v}^{max}$. The favorable agreement between the Navier-Stokes simulations and LST indicates that the control of separation in these cases with intermediate forcing frequency occurs through the Kelvin-Helmholtz mechanism. This conjecture is confirmed by the Reynolds stress term $R_{ST} = |A_u\, A_v \cos(\Phi_u - \Phi_v)\, \frac{\partial U}{\partial y}|$ (Figure 13): The figure shows that the y-location of the maximum of the Reynolds stress term R_{ST} (solid line) lies close to the y-location of the inflection point of the streamwise mean velocity profile, at which $\frac{\partial U}{\partial y}$ (dashed-dotted line) peaks. This location also coincides with the center peak of the amplitude function of the streamwise velocity component (dashed line in the figure). A similar argument was offered by Diwan and Ramesh[27] who found that the inflectional stability dominates the disturbance dynamics downstream of separation.

Disturbances at frequencies below F_j^+ are suppressed. This suppression also holds for the subharmonic component $0.5\,F_j^+$ (dashed-dotted line in Figure 11), which remains at a low level throughout the domain. Unlike in some of the 2-D simulations by Marxen *et al.*[28] (see their Figure

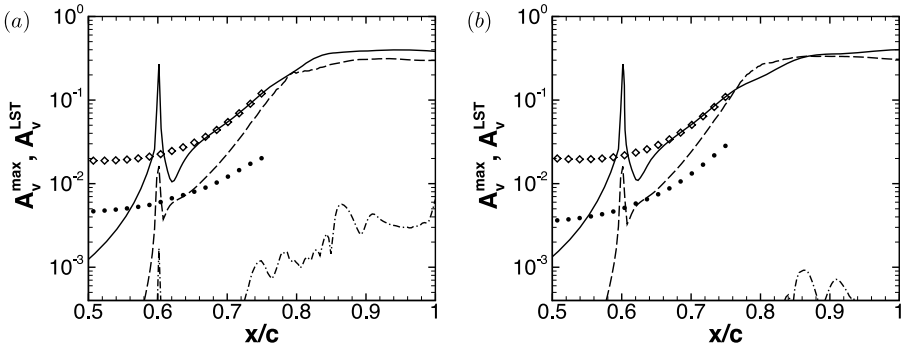

FIG. 11. Results from Navier-Stokes simulations (lines) and LST (based on the respective mean flows, symbols) for (a) case $SJ_{F3.625}$ and (b) case $SJ_{F2.9}$. Amplification curves calculated using Eqs. (3) and (7) for different frequencies, respectively: forcing frequency F_j^+ (—), superharmonic $2\,F_j^+$ (– – –), and subharmonic $0.5\,F_j^+$ (— · —). Results from LST (Eq. (3)) for F_j^+ (◊) and $2\,F_j^+$ (●), respectively, are given as symbols and are scaled so that they match the amplitude from Navier-Stokes simulations.

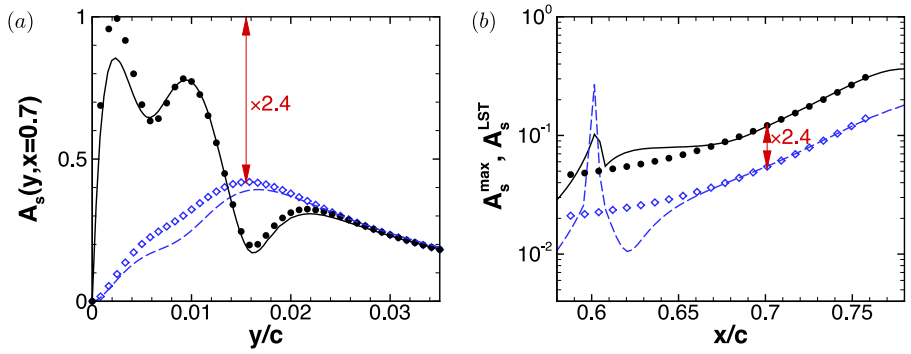

FIG. 12. Results for the streamwise u (—, ●) and wall-normal v velocity components (– – –, ◊) from Navier-Stokes simulation for case $SJ_{F3.625}$ (lines) and LST (symbols) based on the mean flow for case $SJ_{F3.625}$. (a) Amplitude functions at $x = 0.7$, normalized such that A_v matches in the free stream between Navier-Stokes and LST, and the peak value from LST is 1. (b) Amplification curves calculated using Eqs. (3) and (7) for the two velocity components $s = u$ and $s = v$.

21), vortex shedding at a subharmonic frequency does not occur for any of the cases with intermediate actuation frequency. The vortices are shed from the bubble at the actuation frequency in all cases $SJ_{F2.9}$, $SJ_{F3.625}$, and $SJ_{F5.8}$.

The evolution of the first higher harmonic $2F_j^+$ (also contained in Figure 11 for both actuation frequencies) is examined in the following. Two different processes may govern this evolution. First, if LST at the corresponding frequency $2F_j^+$ predicts high amplification rates, the higher harmonic may grow due to the shear-layer instability, in which case the streamwise amplitude evolution will agree with linear stability theory. Such a behavior can be seen for instance in Rist and Augustin[11] (their Figure 7). However, for smaller linear amplification rates, the growth may be caused by non-linear energy transfer, or the quadratic non-linearity in the Navier-Stokes equations. As demonstrated for case $SJ_{F2.9}$ in Figure 14(a), the amplitude for a disturbance with $F^+ = 2F_j^+ = 5.8$ compares well with a line defined as eight times the square of the amplitude of the forced disturbance $8(\hat{v}^{max}_{F_j^+=2.9})^2$, confirming that non-linear energy transfer occurs for case $SJ_{F2.9}$.

Overall, Case $SJ_{F5.8}$ is very similar to cases $SJ_{F3.625}$ and $SJ_{F2.9}$, even though stronger-than-linear growth downstream of $x \approx 0.7$ is observable when the forced disturbance has reached a fairly large amplitude (Figure 14(b)). Non-linearity leads to a self-induced destabilization. This effect may be beneficial for the reattachment efficiency and may explain why this case has the most upstream reattachment location of all cases (see Table I).

In all cases, the saturation of forced disturbances and a corresponding gain in amplitude of its superharmonics is associated with the roll-up of the shear layer. This roll-up is followed by

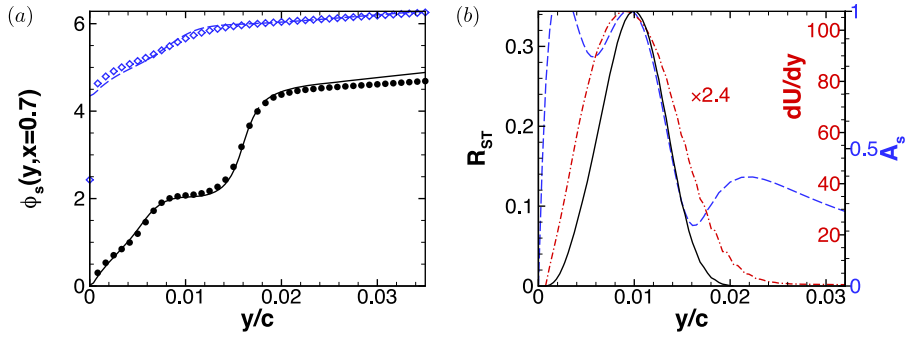

FIG. 13. Results for the streamwise u (—, ●) and wall-normal v velocity components (– – –, ◊) from Navier-Stokes simulation for case $SJ_{F3.625}$ (lines) and LST (symbols) based on the mean flow for case $SJ_{F3.625}$. (a) Phase functions at $x = 0.7$. (b) Reynolds stress term $R_{ST} = |A_u\, A_v \cos(\Phi_u - \Phi_v)\, \frac{\partial U}{\partial y}|$ (—), wall-normal derivative of the streamwise mean velocity $\frac{\partial U}{\partial y}$ (— · —), and normalized amplitude function (– – –), all at $x = 0.7$.

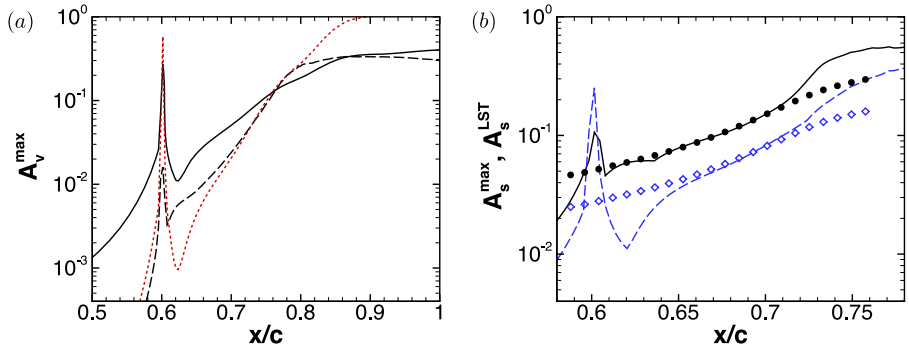

FIG. 14. Amplification curves calculated using Eqs. (3) and (7) from Navier-Stokes simulation (lines) and LST (symbols) based on the respective mean flow. (a) Amplification curves for case $SJ_{F2.9}$ for different frequencies: forcing frequency F_j^+ (—), superharmonic $2\,F_j^+$ (– – –). The dotted line (···) is computed from $8\left(A_v(F_j^+)\right)^2$. (b) Amplification curves for case $SJ_{F5.8}$ for the two velocity components $s = u$ (—, ●) and $s = v$ (– – –, ◊) for the actuation frequency $F^+ = F_j^+ = 5.8$.

pinch-off of vortices and shedding at the respective forcing frequency. This process leads to early reattachment as reported in previous studies of laminar-turbulent transition[9] and active control[11] of laminar separation bubbles. Moreover, absolute instabilities are suppressed in these controlled cases, and the flow behavior is entirely dictated by convective perturbations.

D. Low forcing frequency: Control by the Orr mechanism

If the actuation frequency is decreased further as in the cases $SJ_{F1.45}$, $SJ_{F0.97}$, and $SJ_{F0.725}$, the forced disturbance no longer dictates the flow dynamics directly, specifically the vortex shedding from the bubble. Instead, we observe a behavior that resembles again the cases with very high forcing frequencies. For instance, in case $SJ_{F0.725}$ the forced perturbation is initially convectively amplified and a favorable agreement with LST is seen (Figure 15(a)). Eventually, a disturbance with frequency $F^+ = 2.9$, the same frequency that dominated the uncontrolled case, quickly emerges and reaches a high amplitude at the downstream end of the airfoil, $x \approx 1$. Hence, Figure 15(a) is similar to Figure 9(a), which belongs to case $SJ_{F11.6}$.

The location of explosive growth and the saturation level for the disturbance with $F^+ = 2.9$ in case $SJ_{F0.725}$ resemble those of the uncontrolled case *noSJ* (compare the two different dashed lines in Figure 15(b)). However, unlike case *noSJ*, a perturbation with $F^+ = 3.625 = 5\,F_j^+$ emerges even slightly upstream of the rise of $F^+ = 2.9$, and the former is the first perturbation to reach a very high amplitude (dashed-dotted line in Figure 15(b)). This change in absolute frequency can

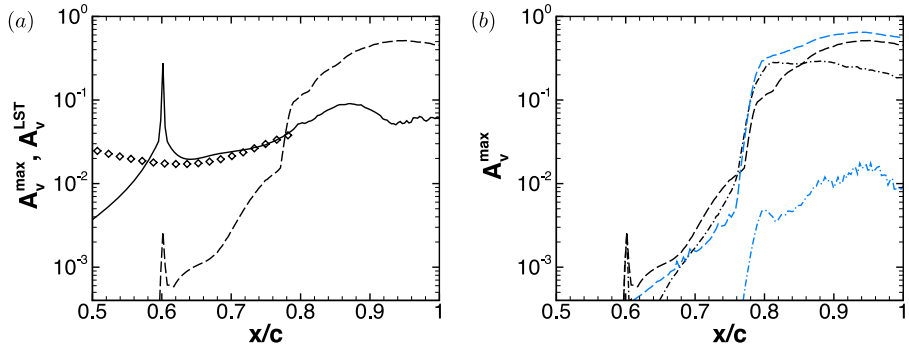

FIG. 15. Amplification curves $A_v = \hat{v}_k^{max}(x)$ for different frequencies. (a) Numerical results from case $SJ_{F0.725}$ for $F^+ = 0.725$ (—) and $F^+ = 2.9$ (– – –). Results from LST (Eq. (3)) for the forcing frequency $F^+ = 11.6$ are given as symbols and are scaled so that they match the amplitude from numerical simulation. (b) Comparison between numerical results for case $SJ_{F0.725}$ (black lines) and case $noSJ$ (grey/blue lines) for $F^+ = 2.9$ (dashed line) and $F^+ = 3.625$ (— · —).

potentially be explained by several effects. First, the mean flow in the front part of the bubble has changed, possibly shifting the frequency of maximum absolute instability to a different value. Second, triggering of the absolute instability does not depend on the feedback loop as described in Sec. V A anymore. Instead, the absolutely unstable perturbation is seeded by the forcing and its higher harmonics. Therefore, a different, here higher, frequency relative to the uncontrolled case may grow to large amplitudes first.

Cases $SJ_{F0.97}$ and $SJ_{F1.45}$ show essentially the same behavior. In the former, a perturbation with $F^+ = 3.88 = 4\,F_J^+$ is the first to reach a very high amplitude before being overtaken by the disturbance with $F^+ = 2.9$ (not shown). In case $SJ_{F1.45}$ a perturbation with $F^+ = 4.35 = 3\,F_J^+$ saturates first and continues to dominate the flow field. In all three cases with low actuation frequency, the x-location of the explosive growth is approximately the same as in the unforced case.

As shown in Figure 15(a), the agreement between the forced disturbance in the Navier-Stokes simulations and LST in case $SJ_{F0.725}$ is favorable. However, inspection of the wall-normal amplitude functions reveals that the agreement is less satisfactory than for instance in case $SJ_{F3.625}$. When normalized such that the amplitude function for the wall-normal velocity matches in the free stream, the amplitude function for the streamwise velocity in the numerical simulation reaches much larger peak values compared to LST results (Figure 16(a)). In the simulation, $|\hat{u}_k^{max}|$ and $|\hat{v}_k^{max}|$ are almost an order of magnitude apart, while LST results only show a ratio of approximately six as indicated by the arrow in the figure.

Further clarification can be derived from the streamwise evolution of the maximum amplitude $\hat{u}_k^{max}(x)$, in addition to $\hat{v}_k^{max}(x)$ (Figure 16(b)). In a region directly downstream of the forcing strip, $\hat{u}_k^{max}$ increases much stronger than suggested by LST, while $\hat{v}_k^{max}$ decays until $x \approx 0.64$. A short region in which $\hat{u}_k^{max}$ increases more appreciably than suggested by LST adjacent to the actuation strip could already be seen for case $SJ_{F3.625}$ (Figure 12(b)). However, the region of $\hat{u}_k^{max}$ growth and $\hat{v}_k^{max}$ decay is much longer in case $SJ_{F0.725}$.

The observed growth of $\hat{u}_k^{max}$ in the region of decaying $\hat{v}_k^{max}$ suggests that a transient-growth-type mechanism is active. In a shear flow, such a mechanism can cause short-time, or near-field, growth in a two-dimensional flow due to the Orr mechanism (for temporal transient growth, this is explained in Ref. 29). In our case, the Orr mechanism is active in the downstream direction instead of in time (spatial transient growth). Figure 17 visualizes the corresponding process of stretching and clockwise tilting of vorticity due to the action of the shear layer.

For a strongly unstable frequency as in case $SJ_{F3.625}$, exponential growth prevails. If the instability of the forced perturbation is weak, as in case $SJ_{F0.725}$, the transient-growth mechanism dominates, here up to the point where the absolute instability becomes active.

The streamwise disturbance velocity in case $SJ_{F0.725}$ is sufficiently large so that it influences the mean flow in the upstream part of the bubble and with it the separation location (Figure 2(b)) as well as the linear stability characteristics (Figure 4(d)). This influence comes from the local, direct effect of quadratic non-linearity, which does not only cause higher harmonics but also affects the mean flow. This renders the control mechanism different to the one of medium-frequency cases

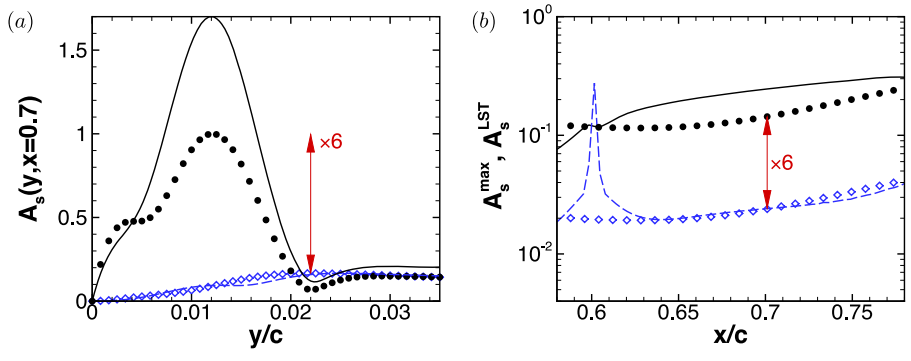

FIG. 16. Same as Figure 12, but for case $SJ_{F0.725}$.

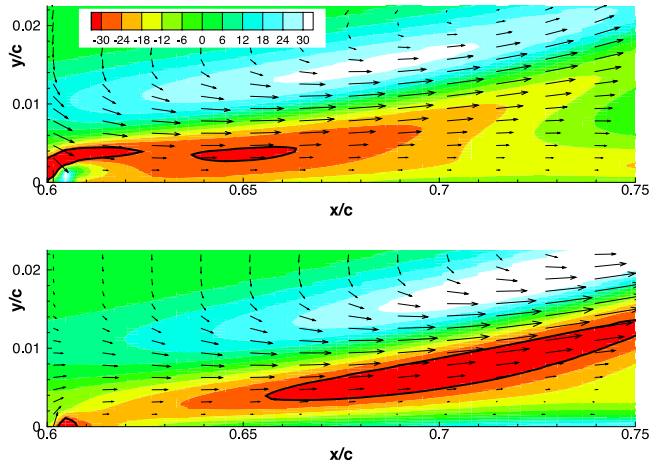

FIG. 17. Disturbance vorticity contours for $F^+ = 0.725$ from Navier-Stokes simulation, case $SJ_{F0.725}$, together with disturbance velocity vectors at times T^1 (top) and $T^1 + \left(8\,F_j^+\right)^{-1}$ (bottom).

discussed in Sec. V C. There, it was due to vortices shed from the bubble, together with the effect of the mean flow deformation. Here, on the other hand, it is due to wall-vortex interaction in the upstream part of the bubble (as in Ref. 16).

VI. DISCUSSION

At low actuation frequencies, an inspection of the downstream evolution of the streamwise and wall-normal disturbance velocity components as well as disturbance vorticity contours indicates that transient growth due to the Orr mechanism occurs before the modal instability sets in. The lower the actuation frequency, the more important the transient-growth mechanism becomes. Vortex shedding remains due to an absolute instability as in the uncontrolled case. However, these absolute instabilities are altered in two ways: first, the most amplified frequency may change due to the distorted mean flow caused by the wall-vortex interaction; second, the seeding amplitude for the absolute instabilities depends on the forcing and no longer only on the feedback loop.

For intermediate forcing frequencies, the controlled flow field shows clean features of the effect of mean flow deformation. First, the controlled separation bubble shrinks from both sides. Second, the controlled flow exhibits altered stability characteristics. Moreover, the range of unstable frequencies decreases significantly. The influence of forcing on convective linear instability is particularly pronounced for frequencies around and above the most convectively amplified frequency in the uncontrolled case. In particular, disturbances at very high frequencies are now damped. However, these high frequencies do not play an important role in the flow dynamics in all the cases considered here, since lower frequency perturbations are dominant. Non-linear self-destabilization is observed for a frequency slightly higher than the most amplified one, leading to large amplitudes and quick reattachment in the mean.

If the frequency is too low, the amplification is also not substantial. However, the amplification rate is only slightly reduced by the non-linear effects. Moreover, at low frequency, transient growth due to the Orr mechanism enhances the amplitude of the streamwise velocity component significantly, and the resulting wall-vortex interaction contributes to the control of separation. In particular, the point of separation continues to be located downstream of its original position in the uncontrolled case. Therefore, the control efficiency decreases only gradually with decreasing the frequency of actuation, whereas for high frequencies an abrupt decrease of control efficiency occurs.

In addition to convective instabilities, absolute instabilities play a role in the flow field under consideration. While we did not evaluate absolutely unstable perturbations, a comparison of our base flow with previous studies supports the view that these instabilities can arise. It is likely that the

frequencies for absolute and convective instabilities overlap, but more investigations regarding the nature of the absolute instabilities are required.

VII. SUMMARY AND CONCLUSIONS

In this work, we have applied linear stability theory to examine the effectiveness of separation control for a laminar boundary layer subject to strong adverse pressure gradient on a simplified airfoil. The purpose of the analysis is to explain the relevant mechanisms for separation control and aid in the selection of the actuation frequency for ZNMF control. In order for such analysis to be meaningful, we establish that results from linear stability theory agree well with main trends in the Navier-Stokes simulations. Here, we demonstrate that such good agreement holds for frequencies in the integrally most amplified range, and also for significantly higher and, at least to a certain extent, also for lower frequencies.

The process of shear-layer rollup and vortex shedding occurs for both convectively and absolutely unstable disturbances and independent of the actuation. In the upstream part of the bubble, modal convective instability was detected in all cases, even in the unforced case.

While the uncontrolled flow dynamics are governed by an absolute instability, the most effective control in our configuration is achieved by a convective instability due to the Kelvin-Helmholtz mechanism. Therefore, when selecting the actuation frequency, one should apply convective linear stability analysis in order to determine the optimum actuation frequency instead of forcing at the natural shedding, or absolute, frequency.

Our analysis indicates that two different control mechanisms exist: one is based on Kelvin-Helmholtz shear-layer instability together with the effect of mean flow deformation, and the other exploits the Orr mechanism in conjunction with wall-vortex interaction. For the efficient control of laminar separated flows, the actuation frequency should not substantially exceed the natural flow frequency for two reasons: first, the amplification of high-frequency perturbations is not very strong. Second, due to non-linear effects, the rate is even further reduced making control using high frequencies particularly inefficient.

The smallest separation bubble is observed when the frequency of the actuator matches the integrally most amplified linear stability mode of the controlled base flow (not of the reference configuration). In order to control via convectively unstable boundary-layer waves, it is not sufficient to select the frequency of actuation only. Instead, one should also consider the position of the actuator, e.g., placing the actuator near the location of neutral stability at the actuation frequency.

ACKNOWLEDGMENTS

R.M. would like to acknowledge funding from AFOSR for this work.

[1] R. B. Kotapati, R. Mittal, O. Marxen, F. Ham, D. You, and L. N. Cattafesta III, "Nonlinear dynamics and synthetic-jet-based control of a canonical separated flow," J. Fluid Mech. **654**, 65–97 (2010).
[2] L. E. Jones, R. D. Sandberg, and N. D. Sandham, "Direct numerical simulations of forced and unforced separation bubbles on an airfoil at incidence," J. Fluid Mech. **602**, 175–207 (2008).
[3] M. D. Ripley and L. L. Pauley, "The unsteady structure of two-dimensional steady laminar separation," Phys. Fluids A **5**(12), 3099 (1993).
[4] P. G. Wilson and L. L. Pauley, "Two- and three-dimensional large-eddy simulations of a transitional separation bubble," Phys. Fluids **10**(11), 2932–2940 (1998).
[5] S. Yarusevych, P. E. Sullivan, and J. G. Kawall, "On vortex shedding from an airfoil in low-Reynolds-number flows," J. Fluid Mech. **632**, 245–271 (2009).
[6] T. A. Zaki, J. G. Wissink, P. A. Durbin, and W. Rodi, "Direct computations of boundary layers distorted by migrating wakes in a linear compressor cascade," Flow, Turbul. Combust. **83**(3), 307–322 (2009).
[7] T. A. Zaki, J. G. Wissink, P. A. Durbin, and W. Rodi, "Direct numerical simulations of transition in a compressor cascade: The influence of free-stream turbulence," J. Fluid Mech. **665**, 57–98 (2010).
[8] S. Lardeau, M. Leschziner, and T. A. Zaki, "Large eddy simulation of transitional separated flow over a flat plate and a compressor blade," Flow, Turbul. Combust. **88**(1–2), 19–44 (2012).
[9] O. Marxen and D. S. Henningson, "The effect of small-amplitude convective disturbances on the size and bursting of a laminar separation bubble," J. Fluid Mech. **671**, 1–33 (2011).
[10] D. Postl, W. Balzer, and H. F. Fasel, "Control of laminar separation using pulsed vortex generator jets: Direct numerical simulations," J. Fluid Mech. **676**, 81–109 (2011).

[11] U. Rist and K. Augustin, "Control of laminar separation bubbles using instability waves," AIAA J. **44**(10), 2217–2223 (2006).
[12] C. Bernardini, S. I. Benton, J.-P. Chen, and J. P. Bons, "Pulsed jets laminar separation control using instability exploitation," AIAA J. **52**(1), 104–115 (2014).
[13] J. P. Bons, R. Sondergaard, and R. B. Rivir, "Turbine separation control using pulsed vortex generator jets," J. Turbomach. **123**(2), 198–206 (2001).
[14] M. S. H. Boutilier and S. Yarusevych, "Sensitivity of linear stability analysis of measured separated shear layers," Eur. J. Mech., B: Fluids **37**, 129–142 (2012).
[15] O. Marxen, M. Lang, and U. Rist, "Discrete linear local eigenmodes in a separating laminar boundary layer," J. Fluid Mech. **711**, 1–26 (2012).
[16] M. P. Simens and J. Jimenez, "Alternatives to Kelvin–Helmholtz instabilities to control separation bubbles," in *Power for Land Sea and Air, ASME Proceedings of ASME Turbo Expo 2006*, *Barcelona, Spain*, *8–11 May 2006* (ASME, 2006), Paper No. GT2006-90670, pp. 1191–1199.
[17] O. Marxen and U. Rist, "Mean flow deformation in a laminar separation bubble: Separation and stability characteristics," J. Fluid Mech. **660**, 37–54 (2010).
[18] S. Yarusevych, P. E. Sullivan, and J. G. Kawall, "Airfoil boundary layer separation and control at low Reynolds numbers," Exp. Fluids **38**(4), 545–547 (2005).
[19] D. Simoni, M. Ubaldi, and P. Zunino, "Experimental investigation of flow instabilities in a laminar separation bubble," J. Therm. Sci. **23**(3), 203–214 (2014).
[20] M. S. H. Boutilier and S. Yarusevych, "Separated shear layer transition over an airfoil at a low Reynolds number," Phys. Fluids **24**(8), 084105 (2012).
[21] R. B. Kotapati, R. Mittal, O. Marxen, D. You, V. Kitsios, A. Ooi, and J. Soria, "Harnessing resonant interactions for active control of separated flows," in *Proceedings of the 2006 Summer Program* (Center for Turbulence Research, Stanford University, 2006), pp. 445–456.
[22] R. B. Kotapati, R. Mittal, and F. Ham, "Large-eddy simulations of zero-net-mass-flux jet based separation control in a canonical separated flow," AIAA Paper No. 2008-4085, 2008.
[23] H. Schlichting, *Boundary-Layer Theory* (McGraw-Hill, New York, 1979).
[24] M. Lang, U. Rist, and S. Wagner, "Investigations on controlled transition development in a laminar separation bubble by means of LDA and PIV," Exp. Fluids **36**, 43–52 (2004).
[25] A. McAlpine, E. C. Nash, and M. V. Lowson, "On the generation of discrete frequency tones by the flow around an aerofoil," J. Sound Vib. **222**(5), 753–779 (1999).
[26] M. Alam and N. D. Sandham, "Direct numerical simulation of 'short' laminar separation bubbles with turbulent reattachment," J. Fluid Mech. **410**, 1–28 (2000).
[27] S. S. Diwan and O. N. Ramesh, "On the origin of the inflectional instability of a laminar separation bubble," J. Fluid Mech. **629**, 263–298 (2009).
[28] O. Marxen, M. Lang, and U. Rist, "Vortex formation and vortex breakup in a laminar separation bubble," J. Fluid Mech. **728**, 58–90 (2013).
[29] B. F. Farrell, "Optimal excitation of perturbations in viscous shear flow," Phys. Fluids **31**(8), 2093–2102 (1988).